Transport, vertical structure and radiative properties of dust events in southeast China determined from ground and space sensors

Jianjun Liu [a,b], Youfei Zheng [a], Zhanqing Li [a,b,*], Connor Flynn [c], E.J. Welton [d], Mareen Cribb [b]

[a] Jiangsu Key Laboratory of Atmospheric Environment Monitoring and Pollution Control, Nanjing University of Information Science & Technology, Nanjing, China
[b] Department of Atmospheric and Oceanic Science and Earth System Science Interdisciplinary Center, University of Maryland, College Park, Maryland, USA
[c] Pacific Northwest National Laboratory, Richland, Washington, USA
[d] Goddard Space Flight Center, NASA, Greenbelt, Maryland, USA

ARTICLE INFO

ABSTRACT

Two dust events were detected over the Yangtze Delta region of China during March 14–17 and April 25–26 in 2009 where such dust events are uncommon. The transport behavior, spatio-temporal evolution, vertical structure, direct radiative effects, as well as induced heating rates, are investigated using a combination of ground-based and satellite-based measurements, a back-trajectory analysis, an aerosol model and a radiative transfer model. Back-trajectories, wind fields and aerosol model analyses show that the first dust originated in northern/northwestern China and the second generated in the Taklimakan desert in northwest China, and traveled across the Hexi corridor and Loess Plateau to the Yangtze Delta region (the so-called "dust corridor"). The mean lidar extinction-to-backscatter ratio (LR) during the two dust events was 38.7 ± 10.4 sr and 42.7 ± 15.2 sr, respectively. The mean aerosol depolarization ratio (δ_a) for the first dust event was 0.16 ± 0.07, with a maximum value of 0.32. For the second, the mean δ_a was around 0.19 ± 0.06, with a maximum value of 0.29. Aerosol extinction coefficient and δ_a profiles for the two events were similar: two aerosol layers consisting of dust aerosols and a mixture of dust and anthropogenic pollution aerosols. The topmost aerosol layer is above 3.5 km. The maximum mean aerosol extinction coefficients were 0.5 km^{-1} and 0.54 km^{-1} at about 0.7 km and 1.1 km, respectively. Significant effects of cooling at the surface and heating in the atmosphere were found during these dust events. Diurnal mean shortwave radiative forcings (efficiencies) at the surface, the top-of-the-atmosphere and within the atmosphere were -36.8 (-80.0), -13.6 (-29.6) and 23.2 (50.4) W m^{-2}, respectively, during the first dust event, and -48.2 (-70.9), -21.4 (-31.5) and 26.8 (39.4) W m^{-2}, respectively, during the second dust event. Maximum heating rates occurred at 0.7 km during the first dust event and at 1.1 km during the second dust event, with a maximum value of 2.74 K day^{-1} for each case. This significant atmospheric heating induced by elevated dust aerosol layers can affect convection and stability in the lower troposphere.

Published by Elsevier Ltd.

1. Introduction

Mineral dust aerosols are a particularly important aerosol type because they can induce significant dynamical perturbations of the synoptic flow (Alpert et al., 1998), absorb and scatter radiation to produce intense direct radiative effects, and play an important role as cloud condensation nuclei. The latter can modify the microphysical properties of cloud and indirectly change climate through cloud radiation processes (Forster et al., 2007). Determining the vertical distribution of dust aerosols is crucial because as a strongly absorbing aerosol, it can influence radiative effects at the top-of-the-atmosphere (Gadhavi and Jayaraman, 2006), modify vertical profiles of radiative heating (Ramanathan et al., 2007), change the stability of the atmosphere and affect convective and turbulent motions and clouds (McFarquhar and Wang, 2006). Dust can have a warming or cooling effect depending on where dust layers are above or below more absorbing atmospheric layers (Meloni et al., 2005; Raut and Chazette, 2008).

However, due to limited observations of dust aerosols on a regional and global scale, especially regarding their vertical distribution, its radiative forcing has not been well quantified. Ground-based and space-based instruments, such as the sun photometer from the Aerosol Robotic Network (AERONET), ground-based lidar, the Ozone Monitoring Instrument (OMI), the Moderate

* Corresponding author. State Laboratory of Earth Surface Process and Resource Ecology, College of Global Change and Earth System Science, Beijing Normal University, Beijing, China.
E-mail address: zli@atmos.umd.edu (Z. Li).

Resolution Imaging Spectroradiometer (MODIS), and the Cloud-Aerosol Lidar and Infrared Pathfinder Satellite Observations (CALIPSO), can be used to study dust aerosol properties. Combining measurements from these instruments, we can identify dust aerosol sources and transport route, and characterize columnar and vertical optical properties. In particular, lidar technology can help us understand processes occurring in dust aerosols aloft and understand their vertical variations.

Asian dust is a dominant aerosol component in northern Asia. Northeasterly winds associated with the Asian monsoon and continental anticyclones may transport dust to southern and southeastern Asia. During long-range transport, dust aerosol properties, such as hygroscopicity, may change through chemical reactions with other kinds of aerosols. Elevated dust layers can lead to instantaneous atmospheric heating rates of approximately $1-4 \, \mathrm{K \, day}^{-1}$ (Kim et al., 2010). In recent years, several observational campaigns focusing on aerosols in Asia were carried out, such as the Asian Pacific Regional Aerosol Characterization Experiment (ACE-Asia) field campaign (Shimizu et al., 2004) and the 2008 China–U.S. joint field campaign (Li et al., 2011). Studies regarding spatial, temporal and vertical variations of dust aerosols have been carried out (Shimizu et al., 2004; Zheng et al., 2008; Huang et al., 2008, 2010), as well as studies focused on the long-range transport of Asian dust (Han et al., 2008; Liu et al., 2009). Most of the research focused on dust source areas in northwestern China but few have studied those affecting southeastern China, an area with high aerosol loading, complex combinations of aerosols, and high humidity (Li et al., 2007). There are also fewer lidar systems deployed in this region.

A comprehensive observation campaign, which involved the collection of radiation, aerosol, and cloud data, was conducted at Taihu from March 2008 to December 2009. The site was established at the edge of Lake Taihu (31.702N, 120.358E, 10 m above sea level) surrounded by large cities in the Yangtze Delta region, such as Shanghai (east of the site), Nanjing (west of the site) and Hangzhou (south of the site). The region has intensive industrial and agricultural activities, with high aerosol loading (Li et al., 2007). In this study, we investigate two dust events that occurred in the spring of 2009 over the Yangtze Delta region regarding their: (1) sources and transport over time, using ground-/satellite-based measurements, back-trajectory analysis and an aerosol model, (2) optical properties and vertical distribution, and (3) direct radiative effects and atmospheric heating rates.

Brief descriptions of the ground and space-borne instruments and their products, as well as the radiative transfer model, are provided in Section 2. In Section 3, dust source identification, transport behavior, vertical properties, as well as direct radiative effects, are described. Finally, a summary is given in Section 4.

2. Observations and methodology

2.1. Ground-based measurements

2.1.1. AERONET sun photometer

An AERONET sun photometer was installed at the Taihu site in 2005 and has been in continuous operation since then (Holben et al., 1998). The instrument takes measurements of direct solar radiance and sky solar radiance at discrete wavelengths to determine the aerosol optical depth (AOD), angstrom exponent α, size distribution and single scattering albedo (SSA) (Dubovik et al., 2002). The uncertainty in AOD is 0.01–0.02, and the SSA for high AOD (>0.4 at 440 nm) at large solar zenith angles ($>50°$) is ~ 0.03. Here, we use the Level 2.0 version of data (calibrated and screened for clouds) as the constraint for MPL retrievals and Level 1.5 data when Level 2.0 data are not available.

2.1.2. Micropulse lidar

The Micropulse Lidar (MPL) in this study is an elastic backscatter lidar developed at the NASA Goddard Space Flight Center (Spinhirne et al., 1995) and manufactured by Sigma Space Corporation, United States, for autonomous aerosol and cloud monitoring with modifications enabling polarization-sensitive measurements (Flynn et al., 2007). The MPL operates at 527 nm, and the laser pulse duration is about 10 ns with a pulse repletion rate of 2500 Hz and output energies in the μJ range. The MPL system has a high vertical resolution (30 m in our study), narrow field of view ($\sim 100 \, \mu \mathrm{rad}$) and narrow interference filters (~ 0.3 nm full width at half maximum, FWHM).

Raw signals acquired by the MPL contain signals from atmospheric molecules (Rayleigh scattering), particles (aerosols and clouds) and quantities associated with background noise (due to sunlight at 527 nm), and instrumental effects (dead time, overlap and afterpulse). In order to retrieve particle properties, the background noise and instrumental effects must be eliminated from the raw signal first. All signal corrections are determined using methods on literatures of Campbell et al. (2002) and Welton and Campbell (2002), excepting afterpulse correction. Details about the afterpulse correction are discussed in an appendix. After all signal corrections are made, the normalized relative backscatter, $P_{NRB}(r)$, also known as NRB, can be obtained. Then the system calibration constant is determined by method of Welton et al. (2002) and the vertical profile of aerosol extinction is determined by the backward Fernald (1984) 2-component solution. The column-averaged aerosol extinction-to-backscatter ratios (LR) are retrieved by constraining lidar-derived AODs to those retrieved from surface sun photometer measurements (Welton et al., 2000). Errors caused by the algorithm and the assumption of a constant LR were tested by Welton et al. (2000).

Alternating every few seconds between transmitting linearly polarized and circularly polarized light, the linear volume depolarization ratio (δ) is computed from the MPL measurement by the method of Flynn et al. (2007). Then the aerosol depolarization ratio, δ_a, is calculated using (Cairo et al., 1999)

$$\delta_a(r) = \frac{R(r)\delta(r)(\delta_m + 1) - \delta_m(\delta(r) + 1)}{R(r)(\delta_m + 1) - (\delta(r) + 1)},$$

where δ_m is the molecular depolarization ratio. R is the backscattering ratio, which is defined as $R(r) = 1 + \beta_a(r)/\beta_m(r)$; $\beta_m(r)$ and $\beta_a(r)$ is the molecular and aerosol volume backscattering coefficient profile, respectively. In our study, δ is used to identify the presence of dust aerosols and δ_a is used to evaluate dust aerosol depolarization properties during the dust events examined here.

2.2. Satellite-based measurements

2.2.1. Ozone monitoring instrument

The OMI instrument employs hyper-spectral imaging in a push-broom mode to measure solar backscattered radiation in the visible and ultraviolet (UV) spectra. It can distinguish between aerosol types, such as smoke, dust, and sulfates, and measures cloud pressure and coverage, which provides data to derive tropospheric ozone column amounts. The OMI aerosol index (AI) measures the wavelength dependence of backscattered UV radiation which helps distinguish dust from other aerosol types because of the high absorption properties of dust in the UV region (Torres et al., 2007). OMI AI information can be used to identify the occurrence of dust events and to understand the transport of dust aerosols from their source location.

2.2.2. Moderate Resolution Imaging Spectroradiometer (MODIS)

MODIS is the key remote sensing instrument deployed onboard NASA's Earth Observing System (EOS) satellites, Terra and Aqua. It

provides high radiometric sensitivity in 36 spectral bands ranging in wavelength from 0.4 μm to 14.4 μm. A ±55-degree scanning pattern at the EOS orbit of 705 km achieves a 2330-km swath and provides global coverage every one to two days. MODIS is a multi-disciplinary instrument designed to measure biological and physical processes, including clouds and aerosols in the atmosphere, sea surface temperature and chlorophyll in the oceans, land cover changes, and so on. In the latest version (collection 005), the algorithm uses a dynamic relationship between the visible surface reflectance (at 470 nm and 660 nm) and the 2130 nm reflectance rather than a fixed relationship (Levy et al., 2007). Some validation studies of this collection show much more accurate AOD retrievals than in previous versions, especially over China (Li et al., 2007). Here, we use MODIS daily Level 2 data, which are produced at a spatial resolution of 10 km × 10 km, to monitor the regional distribution of aerosol optical depths during dust events.

2.2.3. Cloud-Aerosol Lidar and Infrared Pathfinder Satellite Observations (CALIPSO)

The Cloud-Aerosol Lidar and Infrared Pathfinder Satellite Observation (CALIPSO) satellite was launched on April 28, 2006 to study the impact of clouds and aerosols on the Earth's radiation budget and climate. It is used to measure the vertical distributions of aerosols and clouds in the atmosphere, as well as optical and physical properties of aerosols and clouds at 532 and 1064 nm. Equipped with a depolarization channel at 532 nm, discrimination between water and ice clouds is possible, as well as the identification of non-spherical aerosol particles (Winker et al., 2007). Two data products, Level 1 and Level 2, are available at http://www-calipso.larc.nasa.gov/products. Level 1 data includes lidar-calibrated and geo-located profiles, while Level 2 data includes a cloud layer product with different horizontal resolutions, an aerosol layer product at 5-km resolution, and an aerosol profile product with a horizontal resolution of 40 km and a vertical resolution of 120 m. In combination with MPL and OMI AI measurements, Level 2 Vertical Feature Mask data is used to help identify dust aerosols.

2.3. Radiative transfer model

The Santa Barbara DISORT Atmospheric Radiative Transfer (SBDART) model, which is based on the low-resolution band models developed for LOWTRAN 7 atmospheric transmission and the DISORT radiative transfer model (Ricchiazzi et al., 1998), is used to estimate surface shortwave irradiances and to evaluate aerosol direct radiative effects. The model has 33 altitude layers, four radiation streams, and agrees to better than 3% with measurements in the broadband calculation of irradiance (Ricchiazzi et al., 1998). Here, the standard atmospheric profile is used together with ozone and water vapor amounts from OMI and AERONET. Other input include AOD, SSA and asymmetry factor (ASY) at four wavelengths (440, 675, 870, 1020 nm); the aerosol vertical structure is based on MPL retrievals. Surface albedos are taken from the MODIS Level 2 Collection 5 spectral surface reflectance product (MOD09) (Xia et al., 2007). In the model, the Angstrom expression is used to calculate AODs at intermediate wavelengths. We use the method described by Xia et al. (2007) and Li et al. (2010) for computing aerosol direct radiative forcing in the wavelength range of 0.25–4.0 μm. Comparison of surface and top-of-the-atmosphere (TOA) fluxes from SBDART simulations, ground measurements and co-located Clouds and Earth's Radiant Energy System (CERES) satellite retrievals were made by Xia et al. (2007) and Li et al. (2010). Mean bias errors at the surface for direct, diffuse, and global shortwave radiation and global photosynthetically active radiation are 1.2 W m^{-2}, −1.2 W m^{-2}, 6.8 W m^{-2} and 6.9 W m^{-2}, respectively; the agreement in TOA fluxes was compatible in terms of absolute differences. An error analysis showed that the combined error, caused by uncertainties in AOD, Angstrom exponent (α), SSA, ASY, surface reflectance, and ozone amounts, is 8.76 ± 3.44 W m^{-2} (Li et al., 2010).

3. Results and discussion

3.1. Dust event identification and description

Dust aerosols are non-spherical so have a larger linear depolarization ratio than other types of aerosols. Two dust events were observed in the Yangtze Delta region, based on information from ground-based measurements (polarization lidar, sun photometer) and satellite-based observations (OMI, CALIPSO). The first dust event occurred from March 14 to 17, 2009 and the second dust event occurred from April 25 to 26, 2009. Fig. 1 shows the geographical distribution of AI over China from March 14 to 17 (top left) and from April 25 to 26 (bottom left). Pockets of highly absorbing aerosols can be seen during the first dust event, mainly in northern and northwestern China (Xinjiang, Inner Mongolia, Hebei and Shandong provinces) and in southern China. The right-hand panels of Fig. 1 show the paths taken by CALIPSO over China and the vertical feature mask products from March 14 to 16, 2009. The latter shows the presence of dust aerosols over regions with large AI values. During the second dust event, large AI values are predominantly located over the Taklimakan desert and the Yangtze River Delta region (bottom left panel of Fig. 1). Both Taklimakan and Gobi deserts in the north and northwest of China are major sources of dust in East Asia, with long-range transport enabled by either northeasterly winds associated with the Asian monsoon or continental anticyclones associated with the Mei-Yu front in the spring (Lee et al., 2006). The geographic distribution of dust during April 25–26 is similar to that reported in Liu et al. (2008). A 'dust corridor' extended from dust source areas across the Hexi region and Loess Plateau to southeastern China.

Fig. 2 shows the time series of AOD at 440 nm and angstrom exponent α at 440–675 nm (left panels), as well as the mean aerosol volume size distribution (right panel) for the first dust event. The parameter α provides a measure of how rapidly AOD changes with wavelength and the size of aerosol particles (Hansell et al., 2003). AOD and α varied from day-to-day during the period of March 14–17. A relatively low aerosol loading (0.45 ± 0.02 − Table 1) was seen on March 14 and March 15. Mean α decreased from 1.13 ± 0.11 on March 14 to 0.70 ± 0.07 the following day, indicating an increase in the concentration of coarse particles. On March 16, aerosol loading jumped to 0.93 ± 0.08 and daily-averaged α was 0.52 ± 0.03. A transition to high concentrations of anthropogenic aerosols (mean AOD = 1.10 ± 0.24, mean α = 1.10 ± 0.21) was seen on March 17. Over the course of the first dust event, mean AOD and mean α were 0.61 ± 0.21 and 0.91 ± 0.28, respectively. The right-hand panel of Fig. 2 shows that variations in mean aerosol volume size distributions from March 14 to 17 were consistent with variations in AOD and α over that period of time. Fig. 3 shows the cross-sections of NRB and the logarithm of δ from MPL measurements taken during March 14–17, 2009. In our study, a layer contaminated by dust was defined where $\delta > 0.1$ (Cavalieri et al., 2010). On March 14, a thin layer contaminated by dust is seen at low altitude, preceding the peak of the dust event. From 00:00 on March 15 to 06:00 on March 16, multiple elevated dust affected layers were observed. During this period, dust affected layers reached altitudes above 5 km. After 06:00 on March 16, large δ, with values around 0.3, and large NRB values were found at low altitude, indicating an outburst of dense dust. Although the relative concentration of dust aerosols decreased after the dense dust period, the large NRB and δ values on March 17
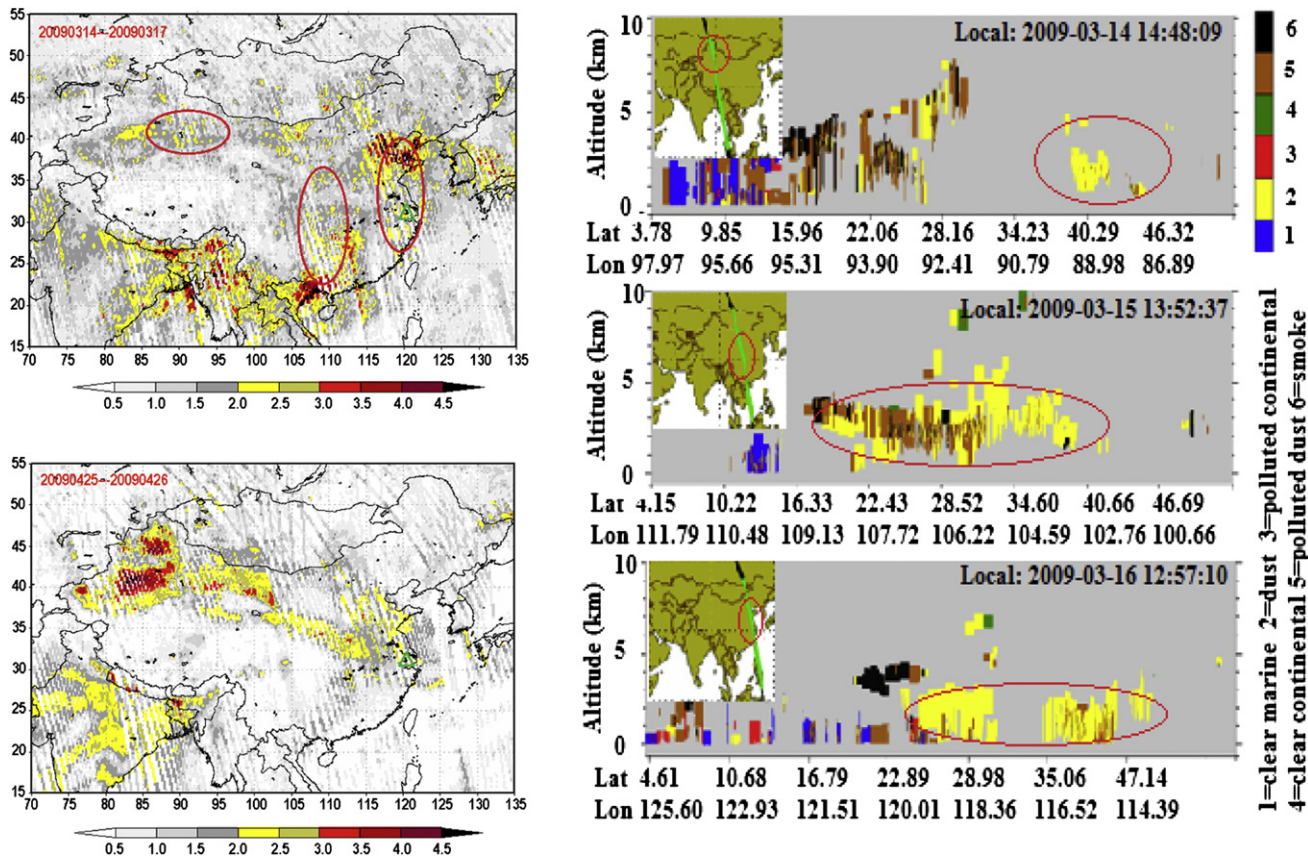
Fig. 1. Aerosol index from OMI for two dust events over China: March 14–17, 2009 (top left) and April 25–26, 2009 (bottom left). Triangular symbol shows the location of the Taihu site. Right images show the vertical feature mask from CALIPSO for the first dust case, where the red circles delineate the same areas also circled in red in the upper left plot.

also indicated the presence of a mixture of dust and spherical particles, such as anthropogenic pollutants.

Fig. 4 shows the time series of AOD and α, as well as the mean aerosol size distribution, for the second dust event. The aerosol loading decreased in magnitude from 1.10 ± 0.12 on April 25 to 0.64 ± 0.05 on April 26; mean α increased from 0.36 ± 0.12 to 1.04 ± 0.11 during this time (see Table 1). This suggests that the relative concentration of coarse particles decreased compared to the concentration of fine particles, or pollutants from the first day to the next. This is also reflected in the change in the averaged aerosol volume size distribution over these two days (right panel of

Fig. 4). Fig. 5 shows the vertical distribution of backscattering properties and the logarithm of δ for this dust event as detected by the ground-based MPL (left panels) and the CALIPSO vertical feature mask (right panel). Relatively heavy dust aerosol loading extended from the surface to about 3 km on April 25. On April 26, δ was slightly greater than 0.1 from the surface to 3 km, indicating that a mixture of dust aerosols and other spherical particles dominated the area. During the entire dust event, an elevated dust contaminated layer was detected above 5 km. This is also seen in the vertical feature mask on April 26 near the site, which shows that there were two distinct dust contaminated layers in the
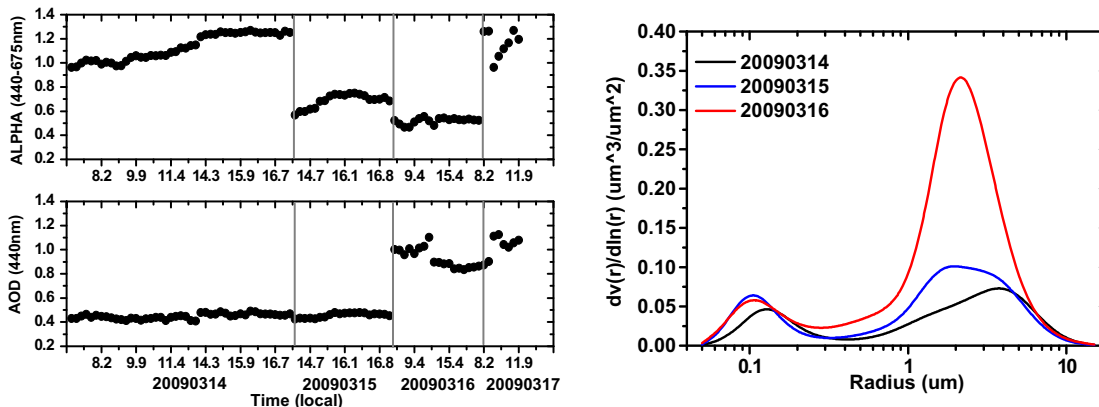

Fig. 2. Time series of AOD at 440 nm and α (440–675 nm) derived from sun photometer data (left panels) and average aerosol volume size distributions (right panels) for the first dust event.

Table 1
Summary of daily mean aerosol optical properties during each dust event.[a]

Dust event		AOD	α	LR (sr)[b]	δ_a[c]
March	14	0.45 ± 0.02	1.13 ± 0.11	$34.2 \pm 4.6(1.3)$	$0.15 \pm 0.04(0.26)$
14–17	15	0.45 ± 0.02	0.70 ± 0.07	$37.2 \pm 9.3(1.1)$	$0.19 \pm 0.05(0.28)$
	16	0.93 ± 0.08	0.52 ± 0.03	$45.2 \pm 12.1(1.8)$	$0.21 \pm 0.04(0.32)$
	17	1.10 ± 0.24	1.10 ± 0.21	$43.1 \pm 1.6(1.3)$	$0.12 \pm 0.02(0.13)$
	14–17	0.61 ± 0.21	0.91 ± 0.28	$38.7 \pm 10.4(1.3)$	0.16 ± 0.06
April	25	1.10 ± 0.12	0.36 ± 0.06	$45.8 \pm 16.0(1.6)$	$0.20 \pm 0.04(0.29)$
25–26	26	0.64 ± 0.05	1.04 ± 0.11	$41.9 \pm 15.0(1.8)$	$0.17 \pm 0.07(0.27)$
	25–26	0.79 ± 0.23	0.81 ± 0.33	$42.7 \pm 15.2(1.8)$	0.19 ± 0.07

[a] AOD at 440 nm; α at 440–675 nm; LR at 527 nm.
[b] Numbers in parentheses represent the average retrieval error (unit: sr).
[c] Numbers in parentheses represent the maximum columnar averaged value.

atmosphere. The presence of a clearly defined gap between the elevated dust contaminated layer and a dust contaminated layer located lower in the atmosphere was found, which is important to consider because assessment of the radiative forcing of dust is affected by the location of the more absorbing aerosol layer (Meloni et al., 2005; Raut and Chazette, 2008). Due to atmospheric heating by the elevated dust layer, atmospheric inversion can easily form between the elevated dust layer and the relatively clear boundary; this can impede the diffusion of aerosols at low altitude due to capping inversion.

3.2. Source identification and transport behavior

Liu et al. (2009) showed that most major Asian dust events originate from Mongolia and Inner Mongolia and are associated with strong cyclone events and cold air outbreaks. Figs. 6 and 7 illustrate the source and transport properties of the March 14–17 dust event. The gray background in Fig. 6 shows the geographic distribution of AOD at 550 nm derived from the MODIS, the black arrows represent the 850 hPa wind field from NCEP daily mean reanalysis data (grid resolution of 2.5° latitude × 2.5° longitude), and the solid (500 m)/dash (1500 m)/dash dot (3000 m) lines are the 72-h back-trajectories (ending at 24:00 local time), simulated using the National Oceanic and Atmospheric Administration (NOAA) Hybrid Single-Particle Lagrangian Integrated Trajectory (HYSPLIT) model. Simulations of the evolution of the dust event over time from the Navy Aerosol Analysis and Prediction System (NAAPS) model (http://www.nrlmry.navy.mil/) are shown in Fig. 7. On March 14, large AODs were seen in the southern and south-western regions of China. Wind was blowing from the northwest

part of China, transporting dust toward the east and over the Yangtze Delta region. The back-trajectory analysis indicates that the airmass over Taihu was from northwestern China, which is in line with the wind field. Model simulations also show that the dust originated from north/northwestern China on March 12, and was then transported to eastern and southern China on March 14 (upper panels of Fig. 7). On March 15, relatively large AODs asso-ciated with dust aerosols (see the AI distribution and CALIPSO vertical feature mask in Fig. 1) were found over southern and northern China. The wind field over southern China shows that a southwesterly airflow was in place, carrying dust aerosols northward. The back-trajectory shows that at high altitude, the airmass mainly came from the western/northwestern region of China (green line in Fig. 6). The surface airmass (red line in Fig. 6) from Mongolia headed toward southern China then veered north with the southwesterly airflow. The results of back-trajectory analysis are consistent with the wind field and aerosol model analysis results. Near the Yangtze Delta region, the flow of air from the southwest toward the north converged with air coming from the northwest, producing an upward movement of air. This may partly explain the elevated dust layer present during this part of the dust event. On March 16, the magnitude of AOD was greatest over the northeast area of Sichuan province, southwest of Taihu. The wind field shows that the prevailing winds over the Yangtze Delta region were from the southwest and that in the northwestern dust source region, the wind flow to the north turned eastward along with prevailing westerlies. Back-trajectories at all three altitudes show that the airmass originated from the region southwest of Taihu. Aerosol model results (Fig. 7) illustrate that dust was present to the south/southwest of Taihu from March 14 to 15 and that in general, the amount of dust in South China gradually decreased over time until the end of the dust event. It is considered that the dust in south/southwest of site mainly came from the north and northwest of China according to aerosol model results. The decrease in strength of the more uniform wind field resulted in a reduced updraft over the Yangtze Delta region and may explain the relatively high concentration of dust aerosols at low altitudes over Taihu on March 16. On March 17, AODs with magnitudes exceeding 0.6 were found over southeastern China. Industrial pollutants and smoke are extant over this economically-developed part of China. The southwesterly airflow on this day transported these anthropogenic pollutants into the Yangtze Delta region; the presence of a mixture of residual dust aerosols and anthropogenic pollutants was suggested by MPL measurements of δ.
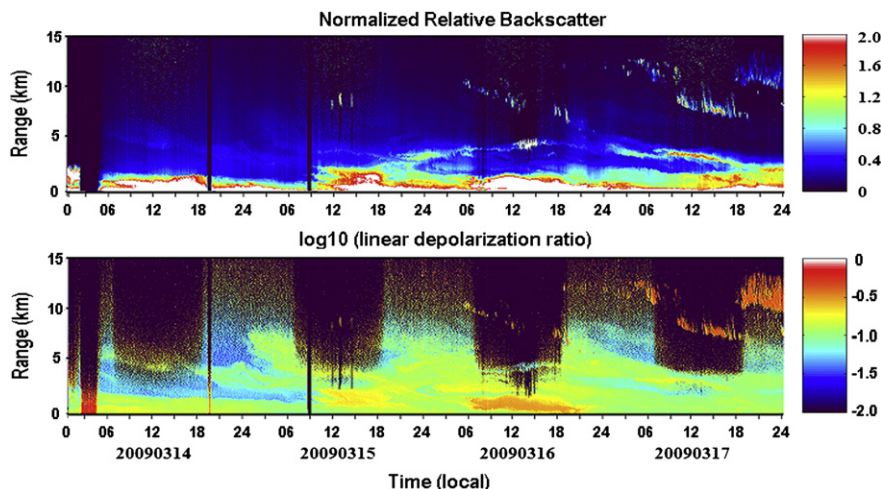

Fig. 3. Normalized relative backscatter and logarithm of linear depolarization ratio images from MPL measurements made at Taihu from March 14 to 17, 2009.
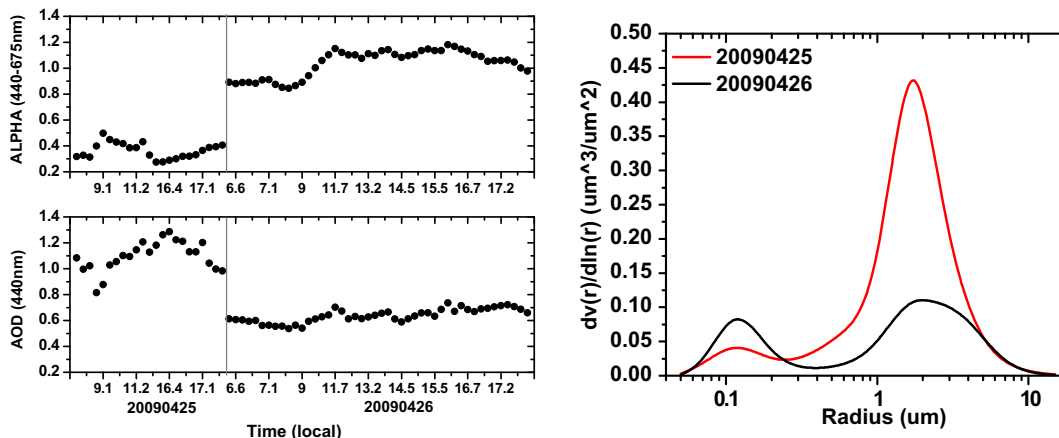
Fig. 4. Same as Fig. 2 but for April 25–26, 2009.

Fig. 8 summarizes the routes taken by dust aerosols during the dust event of March 14–17 observed over the Yangtze Delta region. From March 14 to March 15, dust over the Yangtze Delta region mainly came from north/northwestern China, and was associated with cold temperatures and strong northwesterly winds, induced by continental anticyclones (denoted by (1) in Fig. 8). At the same time, dust was also transported to southern China from north/northwestern China under the influence of the northwesterly airflow (denoted by (2) in Fig. 8). From March 16 to 17, southwesterly winds increased and prevailed over the Yangtze Delta region. Dust entering southern China from via route (2) was diverted to the Yangtze Delta region under the influence of the enhanced southwesterly winds (denoted by (3) in Fig. 8). Overall, changes in the direction of the wind field over the course of the dust event played an important role in dust transport.

Fig. 9 shows the geographical distribution of AOD at 550 nm, and the wind field at 850 hPa, as well as the three-day back-trajectories at 500 m (solid line), 1500 m (dash line) and 3000 m (dash dot line) for the dust event of April 25–26, 2009. The largest values for AOD on April 25 were found in the Yangtze Delta region, with values greater than 1.0, which was associated with dense dust at low altitudes; the magnitude of AOD decreased to 0.6 the following day. Wind directions and back-trajectories show that the low-level airmass mainly came from northeastern China and that the airmass at higher altitudes came from the Taklimakan desert region in northwestern China.

3.3. Aerosol properties measured by the MPL

Table 1 includes column-integrated values of δ_a and the ratio of extinction to backscattering (LR) with retrieval errors. The LR is a key parameter in the backscatter lidar inversion used to derive aerosol optical properties and depends on the aerosol refractive index, size distribution and shape, which changes for different aerosol types. The uncertainties in LR depend on uncertainties in the signal-to-noise ratio, the AOD used to constrain the lidar inversion, the altitude range for normalization and the LR altitude-dependence. In our study, the daily columnar mean LR was 34.2 ± 4.6 sr, 37.2 ± 9.3 sr, 45.2 ± 12.1 sr, and 43.1 ± 1.6 sr from March 14 to March 17, with an average value of 38.7 ± 10.4 sr during the entire period. For the second dust event, the daily columnar mean LR was 45.8 ± 16.0 sr on April 25 and 41.9 ± 15.0 sr on April 26, with an average value of 42.7 ± 15.2 sr for the entire period. The daily-averaged retrieval errors ranged in value from 1.1 sr to 1.8 sr, with an average value of 1.3 sr and 1.8 sr for the two dust events, respectively. LR of dust aerosols have been investigated in many primary dust regions of the world (Voss et al., 2001; Anderson et al., 2003; Matthias et al., 2007; Chiang et al., 2008a; Liu et al., 2008, 2010), some are given in Table 2. In Beijing and Saudi Arabia, for example, the LR values range from 35 sr to 40 sr, and increase toward downstream regions. The relatively large variation of LR indicates the complex nature of aerosol types during dust events.

In the absence of multiple scattering, δ_a is zero for spherical particles and much greater than zero for non-spherical particles. During the four days of the first dust event, the daily mean columnar averaged δ_a was 0.15 ± 0.05, 0.19 ± 0.05, 0.21 ± 0.04 and 0.12 ± 0.03, respectively. The maximum daily mean δ_a occurred on March 16, which is consistent with the evolution of the dust event. The daily columnar averaged δ_a on April 25 and April 26 was 0.20 ± 0.04 and 0.17 ± 0.07, respectively. The averaged δ_a for the
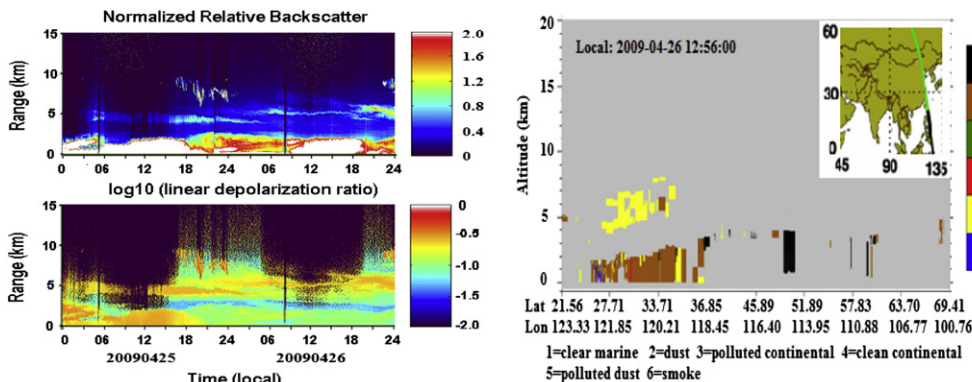

Fig. 5. Normalized relative backscatter and linear depolarization ratio images from MPL measurements made at Taihu during April 25–26, 2009 (left panels), and the vertical feature mask from CALIPSO for April 26, 2009 (right panel). All plots show the presence of dust aerosols.
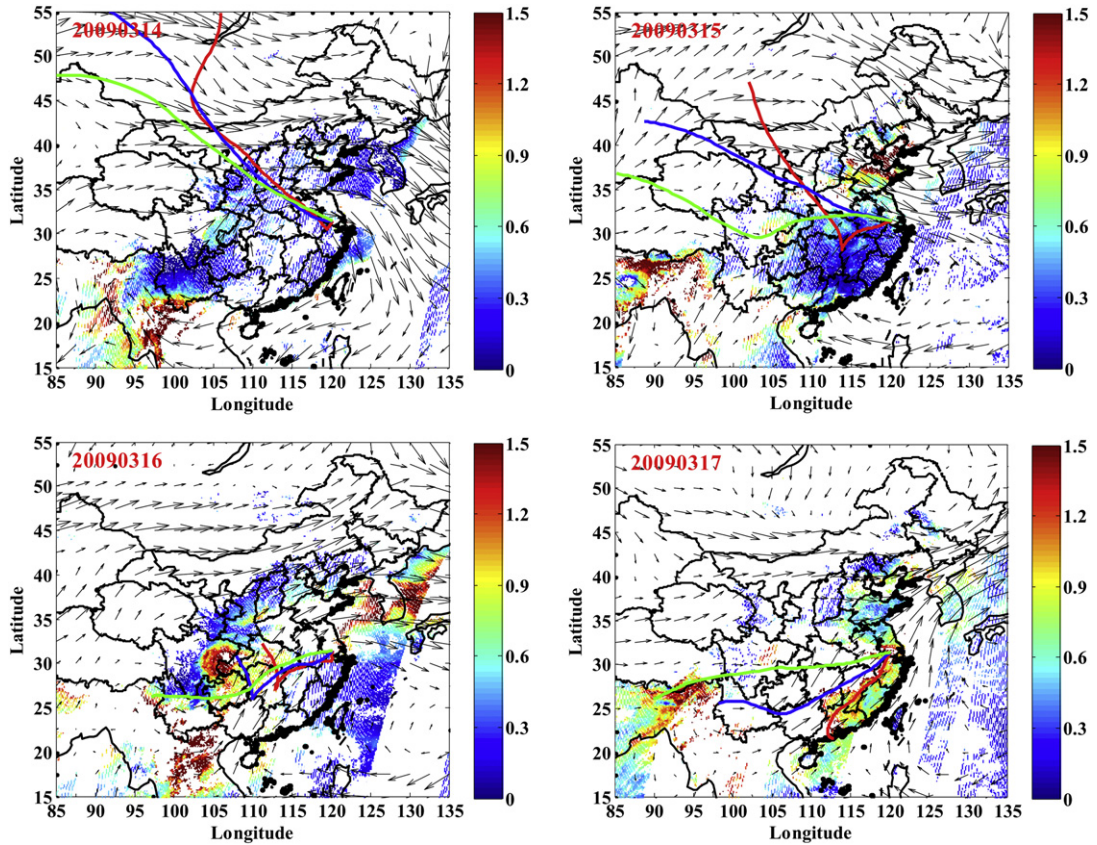
Fig. 6. Geographic distribution of daily AOD at 550 nm derived from MODIS observations (gray background); 850 hPa wind fields (black arrows) from NCEP reanalysis data; 72-h back-trajectories (ending at 24:00 local time), simulated using the National Oceanic and Atmospheric Administration (NOAA) Hybrid Single-Particle Lagrangian Integrated Trajectory (HYSPLIT) model, at 500 m (solid line), 1500 m (dash line) and 3000 m (dash dot line) AGL, respectively.

two dust events was 0.16 ± 0.07 and 0.19 ± 0.06, respectively. These values are in line with δ_a reported in eastern and southeastern Asia by others, e.g. $0.17-0.25$ in Japan (Sakai et al., 2002), 0.18 (Park et al., 2001) and 0.20 (Nee et al., 2007) in Korea and 0.35 in Beijing, China (Sugimoto et al., 2000).

Fig. 10 shows averaged aerosol extinction vertical profiles (black lines) with corresponding standard deviations (gray shaded areas) and averaged δ_a vertical profiles (gray lines) for the first dust event. Generally speaking, the peaks seen in both aerosol extinction and δ_a profiles have a similar vertical distribution, indicating the dominance
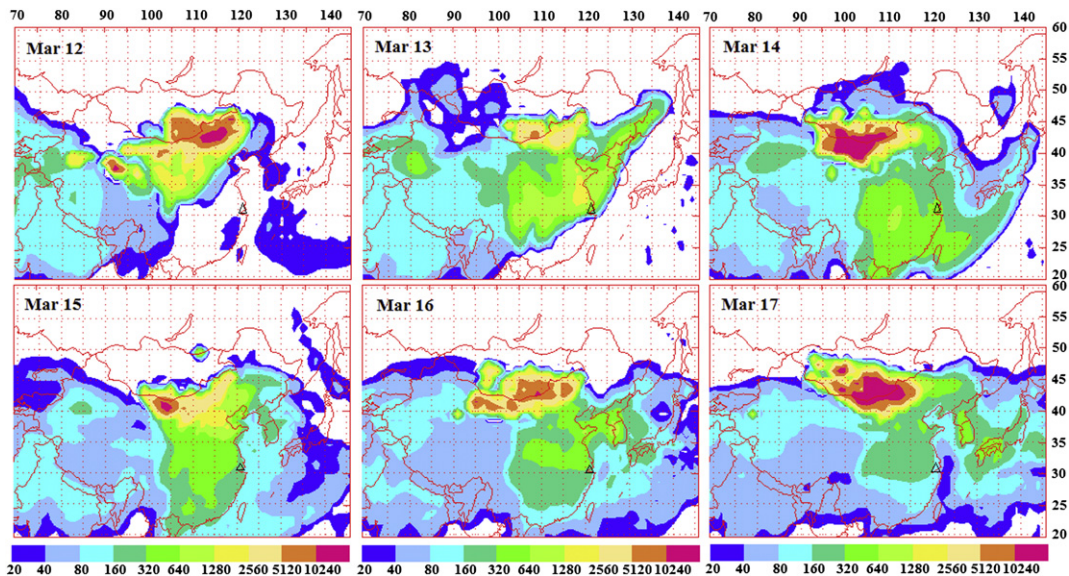

Fig. 7. Spatial distribution of dust concentrations from March 12 to 17, 2009 simulated using the Navy Aerosol Analysis and Prediction System (NAAPS) model. Units are in $\mu g \, m^{-3}$. Triangular symbol shows the location of the Taihu site.
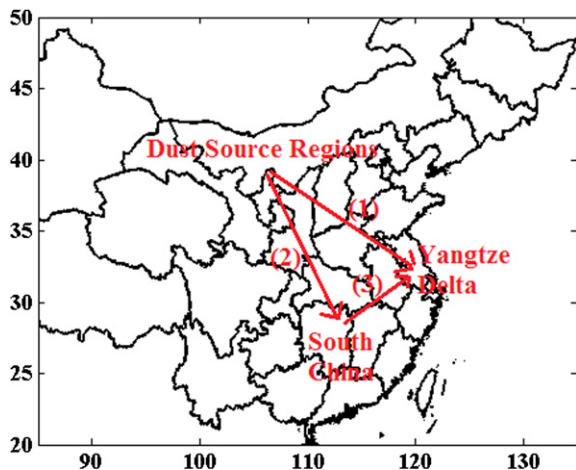
Fig. 8. Different routes taken by Asian dust observed over the Yangtze Delta region from March 14 to 17, 2009.

Table 2
Lidar ratios at 532 nm (LR) from other studies focusing on Asian dust aerosols.

Region	System	LR (sr)	Reference
Tsukuba, Japan	Raman lidar	46 ± 5	Sakai et al., 2002
Tokyo, Japan	Raman lidar	47 ± 7	Liu et al., 2002
Tokyo, Japan	Raman lidar	46 ± 10	Murayama et al., 2003
Western Pacific	In situ measurement	53 ± 5	Anderson et al., 2003
Beijing, China	Raman lidar	40 ± 5	Matthias et al., 2007
Beijing, China	Raman lidar	35 ± 5	Muller et al., 2007
Saudi Arabia	Raman lidar	38 ± 5	Muller et al., 2007
Chung-li, Taiwan	Lidar	44 ± 19	Chiang et al., 2008a,b
Gwangju, Korea	Raman lidar	51 ± 6	Noh et al., 2008

of non-spherical particles in the layer. On March 14, almost all aerosols were located below 2.0 km, with a peak in extinction coefficient (0.17 km^{-1}) at about 0.8 km. From the surface to 2.0 km, δ_a slowly varied in the range of 0.16–0.18. Although the corresponding extinction coefficients were small in magnitude, additional concentrations of dust aerosols were seen at around 2.5 km ($\delta_a \sim 0.25$) and above 4.5 km ($\delta_a \sim 0.2$). On March 15, two relatively large peaks in extinction coefficient are seen at 0.6 km (0.15 km^{-1}) and 1.5 km (0.12 km^{-1}). Large δ_a values are located between 0.8 and 4.3 km, indicating a relatively large proportion of non-spherical particles in total aerosol loadings. An elevated dust layer with a small extinction coefficient and a large δ_a is seen between 3.5 and 4.5 km. The outburst of dense dust (after 06:00 h local time on March 16) was characterized by distinct jumps in magnitude of the extinction coefficient (0.5 km^{-1}) and by large δ_a (larger than 0.35) at altitudes below 2.5 km; dust also appeared at higher altitudes. On March 17, a layer with large extinction coefficient values was located between 3.5 and 4.0 km, with a maximum value of 0.4 km^{-1}. However, relatively large δ_a values were distributed between 3.0 and 3.5 km, with maximum values greater than 0.3. This small discrepancy in the location of maximal extinction coefficient and δ_a values is possibly due to the backscatter lidar retrieval of extinctions is subject to bias in the presence of an inhomogeneous profiles of aerosols using a constant LR with range.

The aerosol extinction coefficient and δ_a vertical profiles for the dust event of April 25–26 are shown in Fig. 11. Two aerosol layers with different vertical distributions and magnitudes of extinction

coefficient and δ_a are seen on each day. On April 25, the first aerosol layer extended from the surface to 2.5 km, with a peak in extinction coefficient (0.54 km^{-1}) at 1.1 km; the second aerosol layer was located between 3.7 and 5.2 km, with a maximum in extinction coefficient (0.1 km^{-1}) at 4.5 km. The vertical distribution of δ_a, which follows that of the extinction coefficient, and the large values of δ_a suggest that non-spherical particles dominated both layers. On April 26, different aerosol types dominated in each aerosol layer. The bottommost layer extended from the surface to 2 km and was characterized by large extinction coefficient values (maximum of 0.18 km^{-1} at 1.65 km) and relatively small δ_a values (around 0.16). This suggests the mixture of dust aerosols mixed with other types of aerosols dominated. The topmost aerosol layer was located between 4.9 and 5.5 km and was characterized by smaller values for extinction coefficient than the lower aerosol layer (maximum of 0.03 km^{-1} at 4.9 km) and larger values for δ_a (maximum of 0.35). It is important to note the presence of elevated dust layers during both dust events. Mineral particles, in general, act as ice nuclei higher up in the atmosphere, so elevated dust layers in Asia may play a much more important role in cloud formation and climate change than the surface dust layer.

3.4. Aerosol radiative effects

Aerosol radiative forcing at top-of-the-atmosphere (TOA) and at the surface (SFC), which is defined as the change in shortwave broadband fluxes (downward minus upward) when aerosols are present with respect to the aerosol-free case, is a commonly used parameter to quantify the direct effects of aerosols on the atmospheric energy budget. Diurnal mean radiative forcing is often expressed as

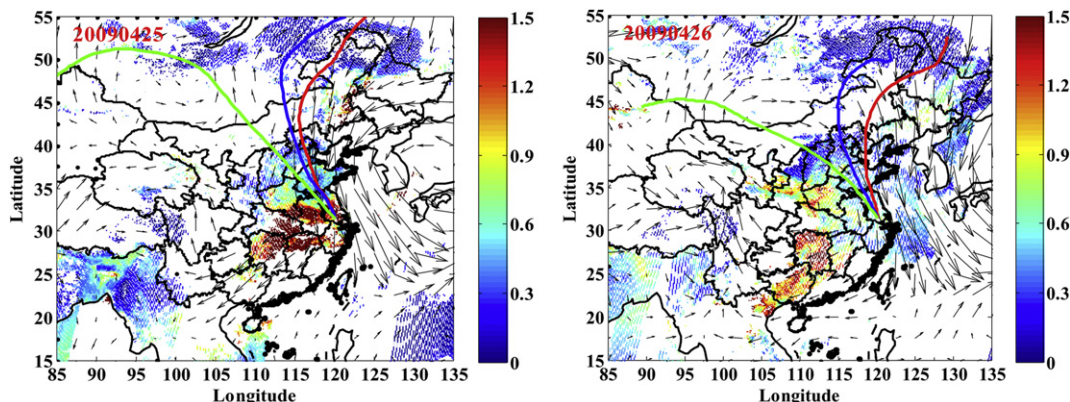$$dF = \frac{1}{24h} \int F(t) dt,$$

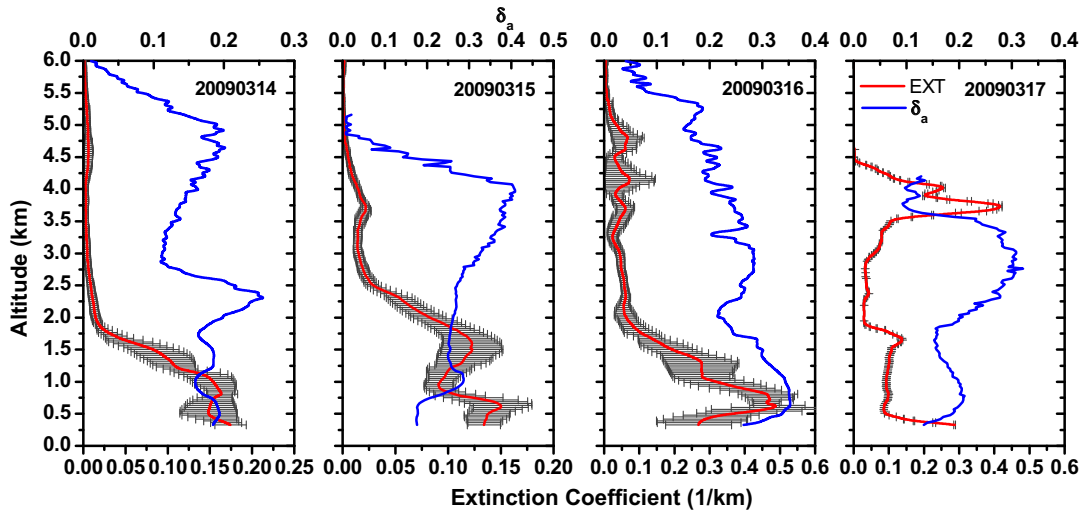**Fig. 9.** Same as Fig. 6 but for April 25–26, 2009.

Fig. 10. Vertical profiles of aerosol extinction coefficient (black lines) and aerosol depolarization ratio (gray lines) on each day of the first dust event.

where $F(t)$ represents instantaneous radiative forcing values (Li et al., 2010). The aerosol atmospheric (ATM) radiative forcing is then defined as the difference between radiative forcings at the TOA and at the SFC. The aerosol radiative forcing efficiency is defined as aerosol radiative forcing per unit AOD, which indicates the effectiveness of aerosols in perturbing the atmosphere. Table 3 shows the diurnal mean radiative forcing (DRF) and the diurnal mean radiative forcing efficiencies (DRFE) at the SFC, TOA and ATM for the two dust events. During the dust event of March 14–17, the DRF at the SFC, TOA, and ATM was −36.8 W m^{-2}, −13.6 W m^{-2}, and 23.2 W m^{-2}, respectively. For the dust event of April 25–26, larger DRF were estimated, namely, −48.2, −21.4 and 26.8 W m^{-2} at SFC, TOA and ATM, respectively. The results indicate a strong cooling effect of dust aerosols at the surface and a significant heating effect within the atmosphere. Comparable values for shortwave diurnal mean radiative forcing at the surface were found at Gwangju, Korea, with values of −52.1 W m^{-2}, −58.4 W m^{-2} and −48.2 W m^{-2} for three dust events (Ogunjobi and Kim, 2008; Bush and Valero, 2003). Pandithurai et al. (2008) estimated that the shortwave aerosol radiative forcing over New Delhi, India during the dust events they studied was −39 W m^{-2} at the SFC and −12 W m^{-2} at the TOA, which is similar to our results. The

DRFE at 550 nm for the two dust events at Taihu is given in Table 3: −80 W m^{-2} and −70.9 W m^{-2} at the SFC, −29.6 W m^{-2} and −31.5 W m^{-2} at the TOA, and 50.4 W m^{-2} and 39.4 W m^{-2} within the ATM, respectively. These are consistent with results from other studies focusing on DRFE during dust events or dust seasons in East Asia. For example, Yoon et al. (2005) showed that the mean forcing efficiency at 500 nm in Gosan, Korea was −80.5 ± 13.2 W m^{-2} and −29.9 ± 4.9 W m^{-2} at the SFC and TOA, respectively. Different studies reported values of −73.0 W m^{-2}, −76.8 ± 10.4 W m^{-2} and −81.1 W m^{-2} at the surface during dust events at the same site, respectively (Bush and Valero, 2003; Won et al., 2004; Ogunjobi and Kim, 2008). During the INDOEX experiment at the Kaashidhoo Climate observatory, DRFE at the surface was −75 W m^{-2} (Bush and Valero, 2002).

Elevated dust layers can lead to significant changes in the atmospheric heating rate (ΔQ, K day^{-1}). For example, Kim et al. (2010) reported that an elevated dust layer can lead to an instantaneous atmospheric heating rate of approximately 1–4 K day^{-1} in the shortwave radiation spectrum, and Alpert et al. (1998) showed that dust may lead to a regional heating rate as large as 6 K day^{-1}. Fig. 12 shows vertical profiles of the mean heating rate for the two dust events at Taihu. Generally speaking, the vertical distribution of mean heating rates is similar to the vertical distribution of mean aerosol extinction coefficients, with maximum values of both quantities located at the same altitude. As the aerosol extinction coefficient increases, the heating rate increases. The maximum heating rates on March 15 and March 16 of the first dust event are about 1.58 K day^{-1} and 2.74 K day^{-1}, respectively; during the two days of the second dust event, maximum heating rates were 2.74 K day^{-1} and 1.91 K day^{-1}, respectively. Aerosol heating rates depend on the aerosol vertical profile and its optical properties, so may have a different range of values in other parts of the world. In their study of dust-related heating rates over northern Africa (10–20N; 20–30E) and southern
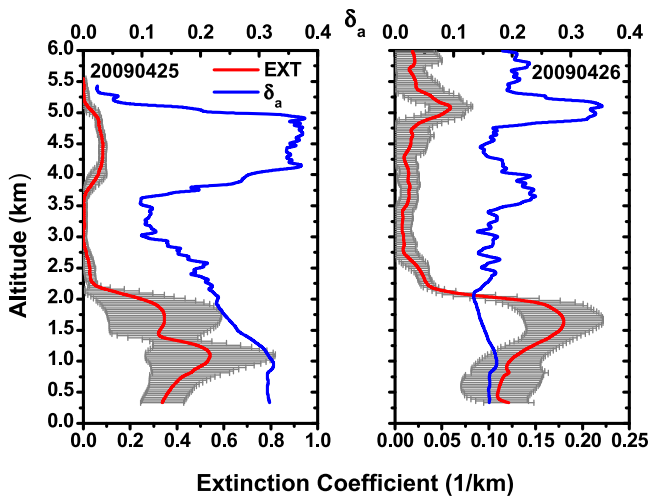

Fig. 11. Same as Fig. 10 but for April 25–26, 2009.

Table 3
The diurnal mean radiative forcing (DRF) and diurnal mean radiative forcing efficiencies (DRFE) at the surface (SFC), the top of atmosphere (TOA) and within the atmosphere (ATM) for the two dust events.

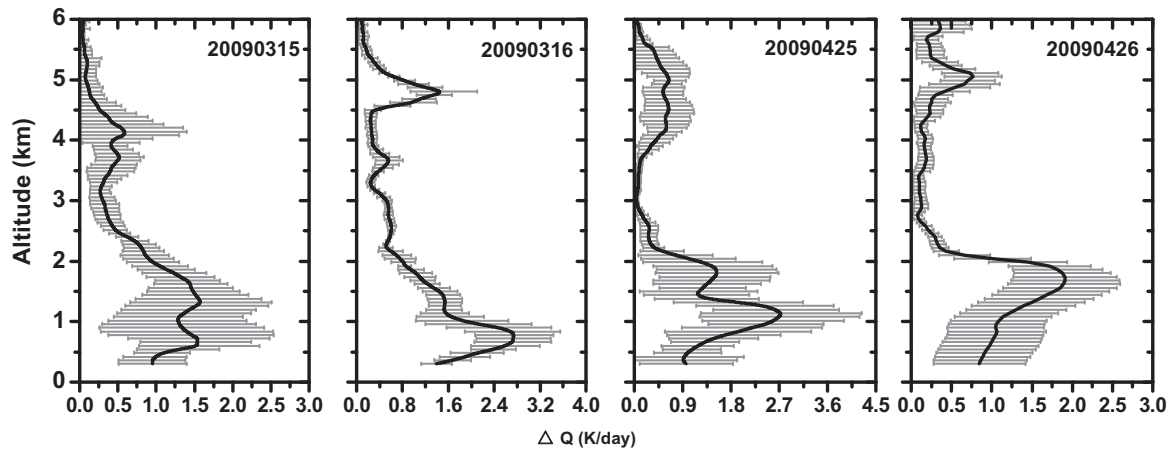|	SFC (W m^{-2})		TOA (W m^{-2})		ATM (W m^{-2})	
	DRF	DRFE	DRF	DRFE	DRF	DRFE
March 14–17	−36.8	−80.0	−13.6	−29.6	23.2	50.4
April 25–26	−48.2	−70.9	−21.4	−31.5	26.8	39.4

Fig. 12. Average heating rate profiles (and standard deviations) on March 15 and March 16 of the first dust event (two leftmost panels) and for the April 25–26 dust event (two rightmost panels).

Africa (10–20S; 20–30E), Satheesh et al. (2006) found that heating rates ranged between 0.4 and 1.2 K day^{-1}. Increased heating rates with increasing height between some altitudes in our study imply a strong impact on convection and the temperature profile. The larger heating rates induced by an elevated dust layer at high altitude would easily form a temperature inversion, which would suppress convection and affect the stability of the lower troposphere (Ramanathan et al., 2007).

4. Conclusions

Two dust events occurred over the Yangtze Delta region, China during March 14–17, 2009 and April 25–26, 2009. The transport behavior, spatio-temporal evolution, vertical structure, direct radiative effects, and atmospheric heating rates characterizing each dust event were investigated over this region using a combination of ground-based and satellite-based measurements made at the Taihu site, a back-trajectory model, an aerosol model and a radiative transfer model. The results are summarized as follows:

Variations of AOD, α, and size distribution, combined with lidar measurements, show the existence and evolution of dust aerosols and mixtures of dust and other pollution aerosols during the two dust events. Back-trajectories, snapshots of the wind field and aerosol model results were used to determine the transport pathways of these dust aerosols. During the first two days of the March dust event, dust aerosols primarily came from northern/northwestern China while on the last two days of the dust event, a shift in wind direction led to an influx of dust aerosols from south/southwest of the Yangtze Delta region, where the dust mainly came from north and northwest China during the first two days. During the dust event of April 25–26, dust aerosols originated from the Taklimakan desert and traveled across the Hexi corridor and Loess Plateau to the Yangtze Delta region.

The average LR for each dust event was 38.7 ± 10.4 sr and 42.7 ± 15.2 sr, respectively. The relatively large variation in values from one dust event to the other suggests the complex nature of aerosol types present. The mean columnar δ_a during the March dust event was 0.16 ± 0.07 with a maximum columnar average value of 0.32, and 0.19 ± 0.06 with a maximum columnar average value of 0.29 during the April dust event. Concerning aerosol extinction coefficient and δ_a profiles during the two dust events, the existence of multiple and elevated dust layers consisting of mixtures of dust aerosols and anthropogenic pollution aerosols was found. In particular, on April 26, an elevated dust layer at 5 km was present

above a mixed aerosol layer that extended from the surface to 2 km. During the outburst of dense dust in the first dust event and on April 25 for the second dust event, the maximum mean aerosol extinction coefficients were 0.5 km^{-1} and 0.54 km^{-1} at about 0.7 km and 1.1 km, respectively.

During the dust event of March 14–17, the DRF at the SFC, TOA, and ATM was -36.8 W m^{-2}, -13.6 W m^{-2} and 23.2 W m^{-2}, respectively, and the corresponding DRFE was -80 W m^{-2}, -29.6 W m^{-2} and 50.4 W m^{-2}, respectively. Larger values for DRF were found during the dust event of April 25–26, namely, -48.2 W m^{-2}, -21.4 W m^{-2} and 26.8 W m^{-2} at the SFC, TOA and ATM, respectively; the corresponding DRFE at the SFC, TOA, and ATM was -70.9 W m^{-2}, -31.5 W m^{-2} and 39.4 W m^{-2}, respectively. The results of our study are consistent with those from other studies made over East Asia and the Yangtze Delta region. Maximum heating rates occurred at about 1.3 km (1.58 K day^{-1}) and 0.7 km (2.74 K day^{-1}) on March 15 and March 16 of the first dust event. During the second dust event, maximum heating rates of 2.74 K day^{-1} and 1.91 K day^{-1} occurred at about 1.1 km and 1.7 km on April 25 and 26, respectively. Atmospheric heating within elevated dust aerosol layers can affect convection and stability in the lower troposphere.

Appendix

The MPL utilizes a co-axial transmitter and receiver designed for eye-safety, and when each laser pulse is triggered, the detector is subjected to an intense initial laser flash from joint optical components. This "noise" signal, referred to as an afterpulse, is time dependent and signals received from atmospheric scattering must be corrected for afterpulse effects. Thus, it is very important to characterize the magnitude of the afterpulse and remove it from the measured signal. Campbell et al. (2002) describe one method to estimate the magnitude of the afterpulse in raw data, which is accomplished when the system operates in a "blocked" configuration, i.e. where atmospheric backscatter and ambient background counts are eliminated. In such a scenario, the signal measured beyond the blocking point (in terms of time) is the sum of the

detector afterpulse and noise; the latter is predetermined and specified by the manufacturer. Here, we used the same principle of afterpulse correction as in Campbell et al. (2002), but we used the signal when the laser beam was completely attenuated by low cloud or by condensation on the instrument window. Under these conditions, there can be three sources of signal at the detector: 1) the detector noise, 2) the afterpulse signal, and 3) the background signal with no range dependence. The afterpulse signal is obtained by subtracting the noise and background signals from the detector signal.

References

Alpert, P., Kaufman, Y.J., Shay-El, Y., Tanre, D., da Silva, A., Schubert, S., Joseph, J.H., 1998. Quantification of dust-forced heating of the lower troposphere. Nature 395, 367–370.

Anderson, T.L., Masonis, S.J., Covert, D.S., Ahlquist, N.C., Howell, S.G., Clarke, A.D., McNaughton, C.S., 2003. Variability of aerosol optical properties derived from in situ aircraft measurements during ACE-Asia. J. Geophys. Res. 108 (D23). doi:10.1029/2002JD003247.

Bush, B.C., Valero, F.P.J., 2002. Spectral aerosol radiative forcing at the surface during the Indian Ocean experiment (INDOEX). J. Geophys. Res. 107 (D19). doi:10.1029/2000JD000020.

Bush, B.C., Valero, F.P.J., 2003. Surface aerosol radiative forcing at Gosan during the ACE-Asia campaign. J. Geophys. Res. 108 (D23). doi:10.1029/2002JD003233.

Cairo, F., Donfrancesco, G.D., Adriani, A., Pulvirenti, L., Fierli, F., 1999. Comparison of various linear depolarization parameters measured by lidar. Appl. Opt. 38 (21), 4425–4432.

Campbell, J.R., Hlavka, D.L., Welton, E.J., Flynn, C.J., Turner, D., Spinhirne, J.D., Scott, V.S., Hwang, I.H., 2002. Full-time, eye-safe cloud and aerosol lidar observation at atmospheric radiation measurement program sites: instrument and data processing. J. Atmos. Ocean. Technol. 19, 431–442.

Cavalieri, O., Cairo, F., Fierli, F., et al., 2010. Variability of aerosol vertical distribution in the Sahel. Atmos. Chem. Phys. Discuss. 10 (7), 17609–17655.

Chiang, C.W., Das, S.K., Nee, J.B., 2008a. Lidar depolarization measurements for aerosol source and property studies over Chungli (24.58° N, 121.1° E). Atmos. Res. 90 (2–4), 203–210.

Chiang, C.W., Das, S.K., Nee, J.B., 2008b. An iterative calculation to derive extinction-to-backscatter ratio based on lidar measurements. J. Quant. Spectrosc. Radiat. Transf. 109, 1187–1195.

Dubovik, O., Holben, B.N., Eck, T.F., Smimov, A., Kaufman, Y.J., King, M.D., Tanre, D., Slutsker, I., 2002. Variability of absorption and optical properties of key aerosol types observed in worldwide locations. J. Atmos. Sci. 59, 590–608.

Fernald, F.G., 1984. Analysis of atmospheric lidar observations: some comments. Appl. Opt. 23, 652–653.

Flynn, C.J., Mendoza, A., Zheng, Y., Mathur, S., 2007. Novel polarization-sensitive micropulse lidar measurement technique. Optic. Express 15 (6), 2785–2790.

Forster, P., et al., 2007. Changes in atmospheric constituents and in radiative forcing. In: Solomon, S., et al. (Eds.), Climate Change 2007: The Physical Science Basis, Working Group I to the Fourth Assessment Report of the Intergovernmental Panel on Climate Change. Cambridge Univ. Press, Cambridge, UK, pp. 129–234.

Gadhavi, H., Jayaraman, A., 2006. Airborne lidar study of the vertical distribution of aerosol over Hyderabad, an urban site in central India, and its implication for radiative forcing calculations. Ann. Geophys. 24 (10), 2461–2470.

Han, Y., Fang, X., Zhao, T.L., Kang, S.C., 2008. Long range trans-Pacific transport and deposition of Asian dust aerosols. J. Environ. Sci. 20 (4), 424–428.

Hansell, R.A., Tsay, S., Ji, Q., Liou, K.N., Ou, S.C., 2003. Surface aerosol radiative forcing derived from collocated ground-based radiometric observations during PRIDE, SAFARI, and ACE-Asia. Appl. Opt. 42 (27), 5533–5544.

Holben, B.N., Kaufman, Y.J., Eck, T.F., Slutsker, I., Tanre, D., et al., 1998. AERONET—a federated instrument network and data archive for aerosol characterization. Remote Sens. Environ. 66, 1–16.

Huang, J., Minnis, P., Chen, B., Huang, Z., Liu, Z., Zhao, Q., Yi, Y., Ayers, J.K., 2008. Long-range transport and vertical structure of Asian dust from CALIPSO and surface measurements during PACDEX. J. Geophys. Res. 113, D23212. doi:10.1029/2008JD010620.

Huang, Z., Huang, J., Bi, J., Wang, G., Wang, W., Fu, Q., Li, Z., Tsay, S.C., Shi, J., 2010. Dust aerosol vertical structure measurements using three MPL lidars during 2008 China-U.S. joint dust field experiment. J. Geophys. Res. 115, D00K15. doi:10.1029/2009JD013273.

Kim, S.W., Yoon, S.C., Kim, J.Y., Kang, J.Y., Sugimoto, N.B., 2010. Asian dust event observed in Seoul, Korea, during 29–31 May 2008: analysis of transport and vertical distribution of dust particles from lidar and surface measurements. Sci. Total Environ. 408, 1707–1718.

Lee, C.T., Chuang, M.T., Chan, C.C., Cheng, T.J., Huang, S.L., 2006. Aerosol characteristics from the Taiwan aerosol supersite in the Asian yellow-dust periods of 2002. Atmos. Environ. 40, 3409–3418.

Levy, R.C., Remer, L.A., Dubovic, O., 2007. Global aerosol optical models and application to MODIS aerosol retrieval over land. J. Geophys. Res. 112, D13210. doi:10.1029/2006JD007815.

Li, Z., Chen, H., Cribb, M., Dickerson, R., Holben, B., Li, C., Liu, D., Luo, Y., Maring, H., Shi, G., Tsay, S.C., Wang, P., Wang, Y., Xia, X., Zheng, Y., Yuan, T., Zhao, F., 2007. Preface to special section on East Asian Studies of Tropospheric Aerosols: an International Regional Experiment (EAST-AIRE). J. Geophys. Res. 112, D22S00. doi:10.1029/2007JD008853.

Li, Z., Lee, K.H., Wang, Y., Xin, J., Hao, W.M., 2010. First observation-based estimates of cloud-free aerosol radiative forcing across China. J. Geophys. Res. 115, D00K18. doi:10.1029/2009JD013306.

Li, Z., Li, C., Chen, H., Tsay, S.C., Holben, B., Huang, J., Li, B., Maring, H., Qian, Y., Shi, G., Xia, X., Yin, Y., Zheng, Y., Zhuang, G., 2011. East Asian studies of tropospheric aerosols and impact on regional climate (EAST-AIRc): an overview. J. Geophys. Res. 116. doi:10.1029/2010JD015257.

Liu, Z., Sugimoto, N., Murayam, T., 2002. Extinction-to-backscatter ratio of Asian dust observed with high-spectral-resolution lidar and Raman lidar. Appl. Opt. 41 (15), 2760–2767.

Liu, T.H., Tsai, F., Hsu, S.C., Hsu, C.W., Shiu, C.J., Chen, W.N., Tu, J.Y., 2009. Southeastward transport of Asian dust: source, transport and its contributions to Taiwan. Atmos. Environ. 43 (2), 458–467.

Liu, D., Wang, Z., Liu, Z.Y., Winker, D., Trepte, C., 2008. A height resolved global view of dust aerosols from the first year CALIPSO lidar measurements. J. Geophys. Res. 113 (D16), D16214.

Liu, Z., Winker, D., Omar, A., Vaughan, M., Trepte, C., Hu, Y., Powell, K., Sun, W., Lin, B., 2010. Effective lidar ratios of dense dust layers over North Africa derived from the CALIOP measurements. J. Quant. Spectrosc. Radiat. Transf. 112 (2), 204–213.

Matthias, T., Ansmann, A., Müller, D., Althausen, D., Engelmann, R., Hu, M., Zhang, Y.G., 2007. Particle backscatter, extinction, and lidar ratio profiling with Raman lidar in south and north China. Appl. Opt. 46, 6302–6308.

McFarquhar, G.M., Wang, H.L., 2006. Effects of aerosols on trade wind cumuli over the Indian Ocean: model simulations. Q.J.R. Meteorol. Soc. 132, 821–843.

Meloni, D., di Sarra, A., Dilorio, T., Fiocco, G., 2005. Influence of the vertical profile of Saharan dust on the visible direct radiative forcing. J. Quant. Spectrosc. Radiat. Transf. 93 (4), 397–413.

Muller, D., Ansmann, A., Mattis, I., Tesche, M., Wandinger, U., Althausen, D., Pisani, G., 2007. Aerosol-type-dependent lidar ratios observed with Raman lidar. J. Geophys. Res. 112 (D16). doi:10.1029/2006JD008292.

Murayama, T., Masonis, S.J., et al., 2003. An intercomparison of lidar-derived aerosol optical properties with airborne measurements near Tokyo during ACE-Asia. J. Geophys. Res. 108 (D23). doi:10.1029/2003JD004153.

Nee, J.B., Chiang, C.W., Hu, H.L., Hu, S.X., Yu, J.Y., 2007. Lidar measurements of Asian dust storms and dust cloud interactions. J. Geophys. Res. 112 (D15). doi:10.1029/2007JD008476.

Noh, Y.M., Kim, Y.J., Muller, D., 2008. Seasonal characteristics of lidar ratios measured with a Raman lidar at Gwangju, Korea in spring and autumn. Atmos. Environ. 42 (9), 2208–2224.

Ogunjobi, K., Kim, Y., 2008. Aerosol characteristics and surface radiative forcing components during a dust outbreak in Gwangju, Republic of Korea. Environ. Monit. Assess. 137 (1), 111–126.

Pandithurai, G., Dipu, S., Dani, K.K., Tiwari, S., Bisht, D.S., Devara, P.C.S., Pinker, R.T., 2008. Aerosol radiative forcing during dust events over New Delhi, India. J. Geophys. Res. 113 (D13). doi:10.1029/2008JD009804.

Park, C.B., Kim, J.H., Lee, C.H., 2001. Measurement of Asian dust by using of multiwavelength lidar. Proc. SPIE 4153, 124–131.

Ramanathan, V., Ramana, M.V., Roberts, G., Kim, D., Corrigan, C., Chung, C., Winker, D., 2007. Warming trends in Asia amplified by brown cloud solar absorption. Nature 448. doi:10.1038/nature06019.

Raut, J.C., Chazette, P., 2008. Radiative budget in the presence of multi-layered aerosol structures in the framework of AMMA SOP-0. Atmos. Chem. Phys. 8 (22), 6839–6864.

Ricchiazzi, P., Yang, S.R., Gautier, C., Sowle, D., 1998. SBDART: a research and teaching software tool for plane-parallel radiative transfer in the Earth's atmosphere. Bull. Am. Meteorol. Soc. 79 (10), 2101–2114.

Sakai, T., Shibata, T., Iwasaka, Y., Nagai, T., Nakazato, M., Matsumura, T., Chiki, K., Kim, Y.S., Tamura, K., Troshkin, D., Handi, S., 2002. Case study of Raman lidar measurements of Asian dust events in 2000 and 2001 at Nagoya and Tsukuba, Japan. Atmos. Environ. 36 (35), 5479–5489.

Satheesh, S.K., Deepshikha, S., Srinivasan, J., 2006. Impact of dust aerosols on Earth-atmosphere clear-sky albedo and its short wave radiative forcing over African and Arabian regions. Int. J. Remote Sens. 27 (8), 1691–1706.

Shimizu, A., Sugimoto, N., Matsui, I., Arao, K., Uno, I., Murayama, T., Kagawa, N., Aoki, K., Uchiyama, A., Yamazaki, A., 2004. Continuous observations of Asian dust and other aerosols by polarization lidars in China and Japan during ACE-Asia. J. Geophys. Res. 109, D19S17. doi:10.1029/2002JD003253.

Spinhirne, J.D., Rall, J.A.R., Scott, V.S., 1995. Compact eye safe lidar systems. Rev. Laser Eng. 23, 112–118.

Sugimoto, N., Matsui, I., Liu, Z., Shimizu, A., Tamamushi, I., Asai, K., 2000. Observation of aerosols and clouds using a two-wavelength polarization lidar during the Nauru99 experiment. Sea and Sky 76, 93–98.

Torres, O., Tanskanen, A., Veihelmann, B., Braak, R., Veefkind, J.P., Levelt, P.F., Barthia, P.K., Ahn, C., Seftor, C., 2007. Aerosols and surface UV products from OMI observations: an overview. J. Geophys. Res. 112, D24S47. doi:10.1029/2007JD008809.

Voss, K.J., Welton, E.J., Quinn, P.K., Johnson, J., Thompson, A.M., Gordon, H.R., 2001. Lidar measurements during Aerosol99. J. Geophys. Res. 106 (D18), 821–831.

J. Liu et al. / Atmospheric Environment 45 (2011) 6469–6480

Welton, E.J., Campbell, J.R., 2002. Micropulse lidar signals: uncertainty analysis. J. Atmos. Ocean. Technol. 19 (12), 2089–2094.

Welton, E.J., Voss, K.J., Gordon, H.R., Maring, H., Smirnov, A., Holben, B., Schmid, B., Livingston, J.M., Russell, P.B., Durkee, P.A., Formenti, P., Andreae, M.O., 2000. Ground-based lidar measurements of aerosols during ACE-2: instrument description, results, and comparisons with other ground-based and airborne measurements. Tellus B 52, 635–650.

Welton, E.J., Voss, K.J., Quinn, P.K., Flatau, P.J., Markowicz, K., Campbell, J.R., Spinhirne, J.D., Gordon, H.R., Johnson, J.E., 2002. Measurements of aerosol vertical profiles and optical properties during INDOEX 1999 using micro-pulse lidars. J. Geophys. Res. 107. doi:10.1029/2000JD000038.

Winker, D.M., Hunt, W.H., McGill, M.J., 2007. Initial performance assessment of CALIOP. Geophys. Res. Lett. 34, L19803. doi:10.1029/2007GL030135.

Won, J.G., Yoon, S.C., Kim, S.W., Jefferson, A., Dutton, E.G., Holben, B.N., 2004. Estimation of direct radiative forcing of Asian dust aerosols with sun/sky radiometer and lidar measurements at Gosan, Korea. J. Meteorol. Soc. Jpn. 82, 115–130.

Xia, X., Li, Z., Holben, B., Wang, P., Eck, T., Chen, H., Cribb, M., Zhao, Y., 2007. Aerosol optical properties and radiative effects in the Yangtze Delta region of China. J. Geophys. Res. 112, D22S12. doi:10.1029/2007JD008859.

Yoon, S.C., Won, J.G., Omar, A.H., Kim, S.W., Sohn, B.J., 2005. Estimation of the radiative forcing by key aerosol types in worldwide locations using a column model and AERONET data. Atmos. Environ. 39 (35), 6620–6630.

Zheng, Y., Liu, J., Wu, R.J., Li, Z., Wang, B., Tamio, T., 2008. Seasonal statistical characteristics of aerosol optical properties at a site near a dust region in China. J. Geophys. Res. 113, D16205. doi:10.1029/2007JD009384.